Level-set multilayer growth model for predicting printability of buried native extreme ultraviolet mask defects

Mihir Upadhyaya, Adarsh Basavalingappa, Henry Herbol, Gregory Denbeaux, Vibhu Jindal, Jenah Harris-Jones, Il-Yong Jang, Kenneth A. Goldberg, Iacopo Mochi, Sajan Marokkey, Wolfgang Demmerle, and Thomas V. Pistor

Articles you may be interested in

Focused helium and neon ion beam induced etching for advanced extreme ultraviolet lithography mask repair
J. Vac. Sci. Technol. B **32**, 021602 (2014); 10.1116/1.4868027

Residual-type mask defect printability for extreme ultraviolet lithography
J. Vac. Sci. Technol. B **30**, 06F501 (2012); 10.1116/1.4756934

Growth and printability of multilayer phase defects on extreme ultraviolet mask blanks
J. Vac. Sci. Technol. B **25**, 2098 (2007); 10.1116/1.2779044

Effect of interface treatment with assisted ion beam on Mo-Si multilayer formation for mask blanks for extreme ultraviolet lithography
J. Vac. Sci. Technol. B **25**, 1554 (2007); 10.1116/1.2768604

Printability of nonsmoothed buried defects in extreme ultraviolet lithography mask blanks
J. Vac. Sci. Technol. B **23**, 2860 (2005); 10.1116/1.2135293

Level-set multilayer growth model for predicting printability of buried native extreme ultraviolet mask defects

Mihir Upadhyaya,[a)] Adarsh Basavalingappa, Henry Herbol, and Gregory Denbeaux
College of Nanoscale Science and Engineering, SUNY Polytechnic Institute, Albany, New York 12203

Vibhu Jindal and Jenah Harris-Jones
SEMATECH, Albany, New York 12203

Il-Yong Jang
Samsung Electronics Co., Suwon-Si, Gyeonggi-do 443-742, South Korea

Kenneth A. Goldberg and Iacopo Mochi
Lawrence Berkeley National Laboratory, Berkeley, California 94720

Sajan Marokkey and Wolfgang Demmerle
Synopsys, Mountain View, California 94043

Thomas V. Pistor
Panoramic Technology Inc., Burlingame, California 94010

The availability of defect-free masks is considered to be a critical issue for enabling extreme ultraviolet lithography (EUVL) as the next generation technology. Since completely defect-free masks will be hard to achieve, it is essential to have a good understanding of the printability of EUV mask defects. In this work, two native mask blank defects were characterized using atomic force microscopy (AFM) and cross-section transmission electron microscopy (TEM), and the defect printability of the characterized native mask defects was evaluated using simulations implementing the finite-difference time-domain and the waveguide algorithms. The simulation results were compared with through-focus aerial images obtained at the SEMATECH Berkeley Actinic Inspection Tool (AIT), an EUV mask-imaging microscope at Lawrence Berkeley National Laboratory. The authors found agreement between the through-focus simulation results and the AIT results. To model the Mo/Si multilayer growth over the native defects, which served as the input for the defect printability simulations, a level-set technique was used to predict the evolution of the multilayer disruption over the defect. Unlike other models that assume a constant flux of atoms (of materials to be deposited) coming from a single direction, this model took into account the direction and incident fluxes of the materials to be deposited, as well as the rotation of the mask substrate, to accurately simulate the actual deposition conditions existing inside the ion beam deposition tool. The modeled multilayer growth was compared to the cross-section TEM images through the defects, as well as to the AFM scans for the given defects, and a good agreement was observed between them. © 2015 American Vacuum Society. [http://dx.doi.org/10.1116/1.4913315]

I. INTRODUCTION

Extreme ultraviolet lithography (EUVL) is the leading next generation lithography technology to succeed optical lithography beyond the 16 nm technology node.[1–3] The reflective masks used in EUVL consist of a low thermal expansion material coated with a Mo/Si multilayer and a patterned absorber layer. The availability of defect-free mask blanks is one of the most critical technology gaps hindering the commercialization of EUVL.[2,3] The defects, namely, the pits, bumps, and particles, can originate either on the substrate, during multilayer deposition, or on top of the multilayer stack.[4–6]

The physical structure of a defect produced by a particle within the multilayer coating of an EUVL mask can be complex. In order to determine the smallest particle capable of producing a printable defect, it is crucial to be able to model the growth as well as the printability of the defects accurately. Modeling is also essential in determining strategies to mitigate the printability of such defects by employing various techniques like defect smoothing,[7] multilayer defect compensation technique,[8] or using additional buffer layer,[9] to name a few.

The most commonly used model, namely, the nonlinear continuum model or the Stearns model[10] used to simulate the multilayer growth over a defect, assumes the deposition and etch fluxes to be at near normal incidence to the mask surface (thereby ignoring the shadowing effects due to the defect), which is not the case in modern coating-deposition systems. The model used here takes into account the various tool parameters and deposition conditions which include the angular flux of atoms incident on the substrate, the chamber geometry, and deposition factors such as substrate and target angles; distances between source, target, and substrate; and the rotational speed of the substrate. The model developed here directly characterizes the ion beam deposition tool by evaluating the aforementioned parameters through experiments

[a)] Electronic mail: mihirupadhyaya@gmail.com

and modeling, and simulates the multilayer growth based on the estimated values of these parameters, as will be discussed in the upcoming section.

The model we developed (also true for the Stearns model) overcomes the limitations of other approaches like the single surface approximation (SSA) and the conformal multilayer growth assumption, which attempt to approximate the defect propagation through the multilayer stack. In SSA, the defective multilayer structure is replaced by a single reflecting surface with the shape of the top surface of the multilayer. The conformal multilayer growth approach assumes the defect to be uniformly propagated through the multilayer stack. Both the approximations only hold true for relatively small defects.[10,11]

The aim of our work was to demonstrate the accuracy of the model based on the level-set[12] technique to predict the multilayer growth over the native mask defects. We did this by drawing comparisons between the aerial images obtained using actinic inspection tool (AIT) tool at Lawrence Berkeley National Laboratory (LBNL)[13] and those obtained using the finite-difference time-domain (FDTD) and waveguide simulations that used the level-set modeled multilayer growth as the input.

II. CHARACTERIZATION OF NATIVE DEFECTS ON EUV MASK BLANKS

Once the multilayer deposition process on the mask substrate was complete, the mask blank was analyzed for defects using a Lasertec M7360 inspection tool, which uses light scattering as a means to detect defects present on the substrate surface. The defect locations were marked with the help of fiducials to easily locate the defects for atomic force microscopy (AFM), transmission electron microscopy (TEM), and AIT printability studies. AFM was performed at the defect locations to observe the defect profile on top of the mask blanks. The masks were then sent to LBNL to undergo inspection at the AIT where the aerial images of the defect sites were obtained at multiple focus conditions. TEM cross-section studies were then performed to observe the multilayer deformations created by the defects. The defect profile at the substrate, obtained from the cross-section TEM, was used as one of the inputs into the multilayer growth model.

III. MULTILAYER GROWTH MODEL

The multilayer growth model, we developed,[14,15] looks at the deposition conditions of the Veeco Instruments' Nexus low defect density tool located in the SEMATECH cleanroom facility in Albany, New York. The tool consists of an ion source, Si, Mo, and Ru targets, and an electrostatic chuck to hold the mask substrate. The schematic of the tool is shown in Fig. 1. Argon ions extracted from the ion source strike the target liberating the atoms to be deposited. The sputtered atoms travel to the substrate where they get deposited, creating the multilayer reflector. The mask substrate is electrostatically chucked to the mask fixture, which precisely positions the substrate relative to the target and spins the substrate around its normal direction.
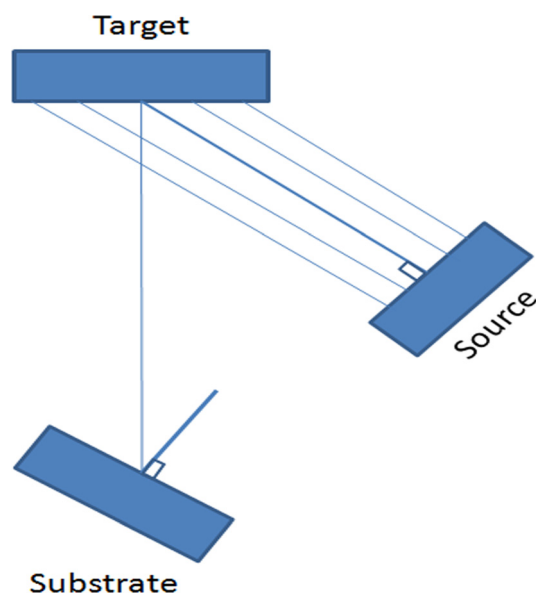
FIG. 1. (Color online) Top–down schematic of the ion beam deposition tool.

Kinetic Monte Carlo simulation methods were used to calculate the angular distribution and energy of the sputtered atoms from the target under exposure of argon ion beam of 300 mA at 600 eV. The sputtered atoms from target were further diffused and scattered inside the chamber to calculate the atomic flux of the atoms reaching the substrate position. The kinetic Monte Carlo method takes into account the probability of striking an ambient gas atom along the atom's trajectory and predicts the energy and direction of the atom after the collision. The scattering gas in the initial simulations was assumed to have a Boltzmann's velocity distribution at 50 °C and to be comprised of argon atoms at 0.14 mTorr, which is the typical pressure inside the Veeco chamber during deposition. Modeling the deposition rate throughout the chamber requires estimates of several parameters, such as the number of atoms ejected from the target at each location on the target, which was estimated using measured target erosion profiles; the angular distribution of atoms reaching the substrate, which was estimated by measuring the deposition rate on substrates mounted on a hemispherical surface around the center of the target; the gas scattering behavior between the target and substrate, which was estimated using a kinetic Monte Carlo method and scattering cross sections. The simulation results were validated by measuring deposition thicknesses from quartz crystal microbalances and wafer coupons placed at different places near substrate position. The details of the experimental and modeling results are reported elsewhere.[15,16] Level-set method was later used to determine the multilayer growth on defect interface with input of sputtered atom flux (of the target materials) reaching the substrate, rotational speed of substrate, and other deposition parameters such as substrate and target angles. The substrate rotation that is commonly used to improve uniformity in the Veeco Nexus tools was modeled to take into account the shadowing effects at defect location. The incoming flux of atoms at substrate surface is directional. The normal flux of atoms reaching at any point

of the surface will not change with time. However, the horizontal flux of atoms at any point will change based on rotational speed and local surface curvature. Further the height and curvature of defect interface at any given time will provide the shadowing effects which can be calculated for every time integral during evolution of surface.

One of the ways to study the evolution of surfaces is by numerically simulating the growth of dynamic implicit surfaces and reproducing multilayer growth on defects. Existing simulation theories can be used such as the fast marching method,[17] front tracking method,[18] and level-set method. The level-set method is a powerful technique based upon an implicit description of evolving surfaces, and, hence, it can account for any topological changes in any number of dimensions. The level-set method was implemented by level-set initialization (interface definition of defect profile on substrate) and development of the level-set (growth of multilayer structure on defect profile) by numerical integration, and level-set visualization. The surface of interest is the contour for which the function $\varphi(r, t)$ is zero. This is called the zero level of the level-set function and describes the surface implicitly. Since the surface is always defined as the same contour of $\varphi(r, t)$, it follows that any level-set function $\varphi(r, t)$ obeys the Hamilton–Jacobi evolution equation given as

$$\frac{d\varphi(r,t)}{dt} + \vec{V}.\nabla\varphi + a|\nabla\varphi| = b\kappa|\nabla\varphi|, \tag{1}$$

where $\varphi(r, t)$ is the definition of the interface given by the initial pit or particle geometry on substrate, $\vec{V}$ is the external velocity vector represented by deposition fluxes reaching the substrate, $\nabla\phi$ defined as $[(d\varphi/dx), (d\varphi/dy), (d\varphi/dz)]$ is gradient of the interface in three dimensions, $\vec{V}.\nabla\varphi$ is deposition by the vector of direct line of sight, $a|\nabla\varphi|$ is deposition due to the flux of atoms reaching the surface by scattering, κ defined as $\nabla \cdot [\nabla\varphi/|\nabla\varphi|]$ is Laplacian of the interface defining the curvature, and $b\kappa|\nabla\varphi|$ represents the evolution of the interface due to the curvature-driven force in the system. a and b are phenomenological constants that depend on the deposition tool and conditions.

The initialization for the level-set method includes initializing a function $\varphi(r,t)$ and setting up boundary conditions. The initialization of the level-set in our case will depend upon the shape of the defect profile on the substrate. Hence, the function was initialized in such a way that the zero level-set represents the shape of defect. The defect profile was defined using the cross-section TEM images through the defect. Further, interface evolution was studied with the discretized level-set data obtained for each time step. The derivative of φ can be approximated by multiple schemes such as first order essentially nonoscillatory (ENO), second or higher order ENO, or weighted ENO. The combination of forward Euler time discretization with the upwinding difference scheme provided a consistent finite difference approximation to the partial derivatives.

The initial defect profile at the mask substrate was defined using the cross-section TEM image through the defect. The process of defect profile definition, which served as an input

into the level-set model, was an iterative one. The outline of the defect shape, as observed in the TEM images was traced and the function defining the traced shape was input into the growth model. The full-width at half-maximum (FWHM) and height of the defect at the top of the multilayer stack, as obtained through the model, were then compared with those as determined by the AFM measurements on top of the multilayer stack. Since the TEM slice may not pass exactly through the center of the defect, the traced outline of the defect could underestimate the FWHM and height of the defect at the substrate, and hence the resulting profile at the multilayer top. So, the bottom defect profile was iteratively adapted until the modeled defect profile matched the AFM defect profile at the multilayer top. This was done since the top few layers of the multilayer structure reflect the majority of the EUV radiation, thus making it critical to model their growth more accurately.

IV. RESULTS

A. Comparing modeled multilayer growth with the cross-section TEM and AFM

Two defects, one bump and one pit, were characterized and studied for this work. The level-set growth model was able to predict the deposition rate and uniformity of the material deposited on the mask substrate. The TEM cross-sections of the defect growth for both the defects (Fig. 3) appear to largely agree with the simulated multilayer growth over the defects. AFM was performed after multilayer deposition to look at the defect profiles on top of the multilayer stack. AFM scans of the defects along with the modeled defect profiles at the multilayer top are shown in Fig. 4. Since the defects studied here are native and nonsymmetric, measurements of FWHM were made along four directions (x-axis, y-axis, and the two 45° diagonals). The AFM measurements of the bump-type defect performed at the top of the multilayer stack yielded a maximum height of 6 nm and an average FWHM value of 58 nm, with a standard deviation of 1 nm. AFM measurements of the pit-type defect at the multilayer top surface yielded a maximum depth of 8 nm and an average FWHM value of 51 nm, with a standard deviation of 4 nm, indicating a non-
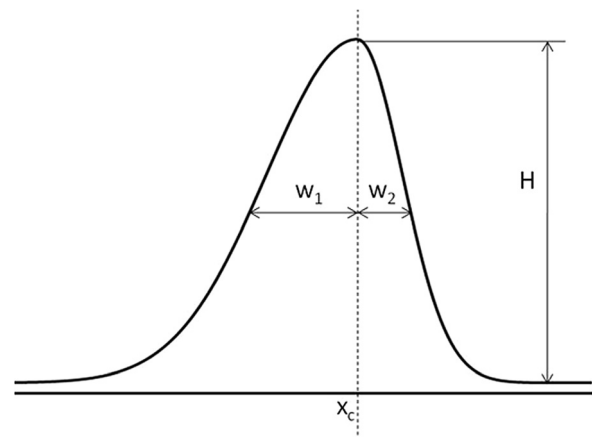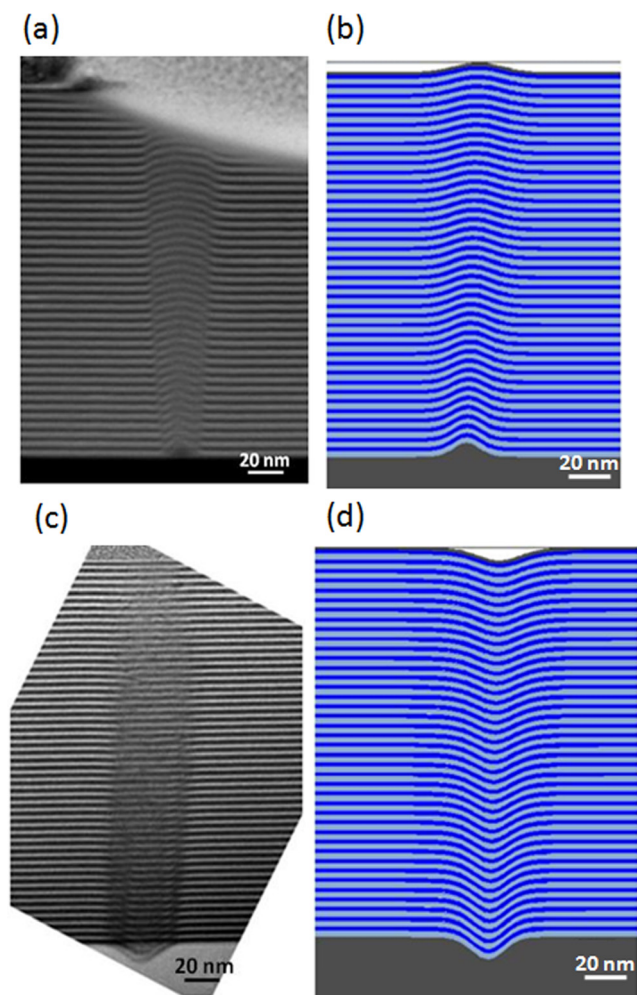
Fig. 2. Illustration of a bi-Gaussian profile.

FIG. 3. (Color online) (a) TEM cross-section of the bump-type defect on the EUV mask. (b) Simulated multilayer growth over the bump-type defect using our model. (c) TEM cross-section of the pit-type defect on the EUV mask. (d) Simulated multilayer growth over the pit-type defect using our model.

rotationally symmetric defect. Even though the asymmetry was about 10%, we modeled a rotationally symmetric defect.

The modeled defect profiles at the multilayer top were in agreement within 1 nm for height and FWHM compared to the average AFM measured profile, after iteratively adapting the substrate defect profiles. The initial substrate defect profiles for both the bump and pit defects, as obtained by tracing the outline of the substrate defects as seen in the cross-section TEM images, were observed to best fit bi-Gaussian profiles as given by

$$y = \begin{cases} He^{-\frac{1}{2}\left(\frac{x_c-x}{w_1}\right)^2} & (x < x_c) \\ He^{-\frac{1}{2}\left(\frac{x-x_c}{w_2}\right)^2} & (x \geq x_c), \end{cases} \qquad (2)$$

where H is the height of the Gaussian, x_c is the position of the center of the peak, w_1 is the FWHM of the half Gaussian function to the left of x_c, and w_2 is the FWHM of the half Gaussian function to the right of x_c. A bi-Gaussian profile has been illustrated in Fig. 2.

The initial substrate defect profiles led to an underestimation of the top-layer FWHM and height/depth compared to the top-layer AFM defect profile. This, we believe is due to the TEM cross-section possibly not being through the center of the defect thereby leading to an underestimation of the substrate defect FWHM and height. Therefore we iteratively increased the defect FWHM and height, keeping the shape of the defect the same, until the modeled multilayer defect profile at the top matched the top-surface AFM defect profile. For the bump defect, the height (H) was increased by 1.7 nm (16%) and FWHM ($w_1 + w_2$) by 4.6 nm (20%) as compared to the height and FWHM of the initial outlined defect respectively to obtain a good match of the top-layer modeled profile with the top-surface AFM scan. Similarly for the pit defect, the depth was increased by 1.2 nm (7%) and FWHM by 3.7 nm (10%) to obtain a good match of the top-layer modeled profile with the top-surface AFM scan.

Multilayer growth of 40 Mo/Si multilayers was modeled with each bilayer being approximately 7 nm thick. The TEM cross-section and modeled cross-section of the multilayer growth over the defects are shown in Fig. 3, and the top-surface AFM scans and modeled multilayer growth of the top-layer are shown in Fig. 4. Although the parameters used here were those of the Veeco Nexus tool, the model can be adapted to simulate multilayer growth under different deposition conditions in different tools.

We finally compared the change of the defect width and height within the multilayer structure between the modeled and the actual multilayer growth. Figure 5 shows a plot of defect FWHM and height as a function of number of bilayers from the mask substrate for the bump defect. In the plot, the lines correspond to the modeled growth and the symbols correspond to the values obtained by tracing the layer contours in the cross-section TEM image of the bump defect. We observe a good agreement between the modeled multilayer growth and the actual multilayer growth, thus giving us confidence in our multilayer growth model. Five measurements were made on the TEM image every six bilayers to extract the mean and the standard deviation in the measurement of FWHM and height of the multilayer growth. The standard deviation (in nanometers) has been shown as error bars in Fig. 5 plot.

B. Comparing the simulation and AIT through-focus aerial images

The simulated multilayer growth was used as the input for the defect printability simulations. To perform the simulations, we used two lithography simulation software packages, namely, Sentaurus Lithography (S-Litho) from Synopsys and EM-SUITE from Panoramic Technology Inc. EM-Suite was used to perform simulations implementing the FDTD algorithm[19,20] while S-Litho was used to perform simulations implementing the FDTD as well as the wave-guide algorithms[21] for the rigorous modeling of EUV masks. The optical and imaging parameters used for the simulations were chosen to match the parameters used for the AIT imaging, which were 13.5 nm wavelength radiation incident on
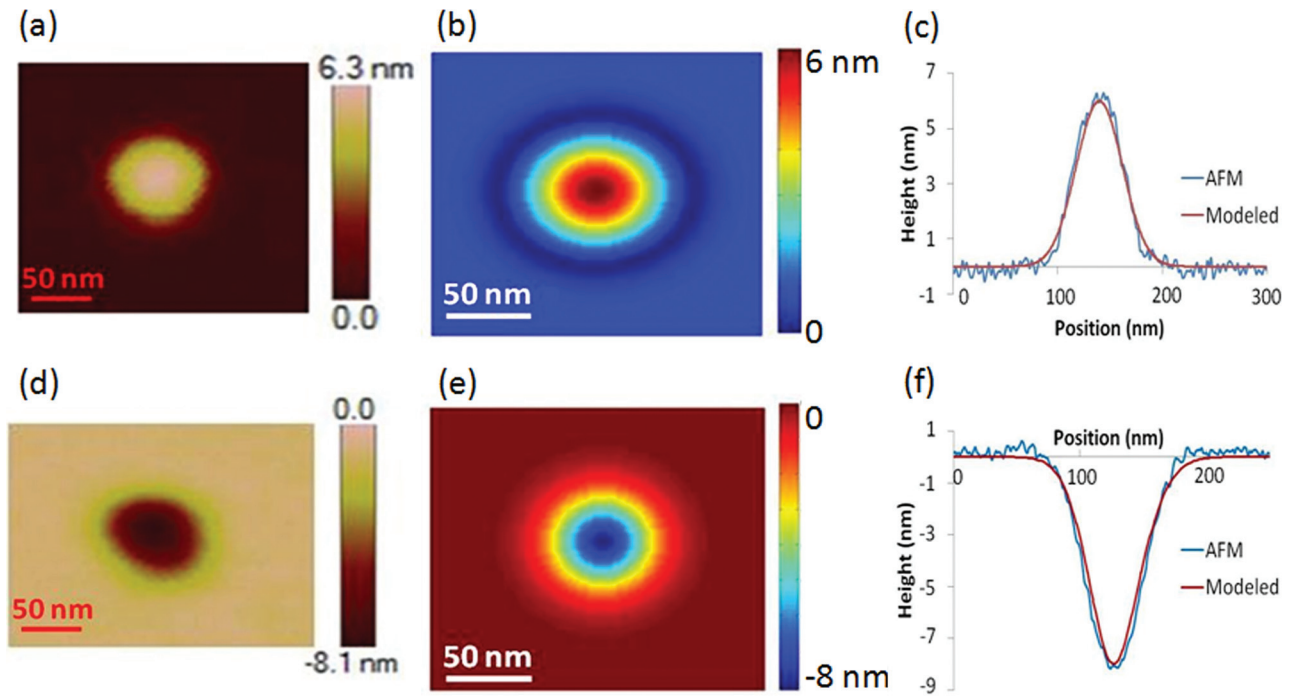
FIG. 4. (Color) (a) AFM image of the bump-type defect at top of the multilayer stack. The bump defect has an average FWHM of 58 nm and a maximum height of 6 nm. (b) Top of the multilayer stack as predicted by level-set multilayer growth model (after iterating bottom defect profile to get agreement with top AFM profile within 1 nm). (c) Plot showing the average of the cross-sections as taken through the four directions of the top-layer AFM and the cross-section as taken through the x-axis of the modeled multilayer growth passing through the maximum height of the bump defect. (d) AFM image of the pit-type defect at top of the multilayer stack. The pit defect has an average FWHM of 51 nm and a maximum depth of 8 nm. (e) Top of the multilayer stack as predicted by level-set multilayer growth model (after iterating bottom defect profile to get agreement with top AFM profile within 1 nm). (f) Plot showing the average of the cross-sections as taken through the four directions of the top-layer AFM and the cross-section as taken through the x-axis of the modeled multilayer growth passing through the maximum depth of the pit defect.

the mask at an angle of 6 degrees, disk-fill illumination with a σ value of 0.2, and a mask-side numerical aperture of 0.0875 (0.35, 4× wafer-side). Figures 6 and 7 show the aerial images from the AIT along with the aerial images obtained using the FDTD and waveguide simulations for the bump-type and pit-type defects, respectively. There is an

arbitrary scaling factor between the AIT-measured aerial image intensities and the aerial image intensities obtained using simulations. These intensities were normalized with respect to the respective average aerial image intensities as obtained from the 2D aerial image intensity maps. Since the defect is a small fraction of the image area and if we assume
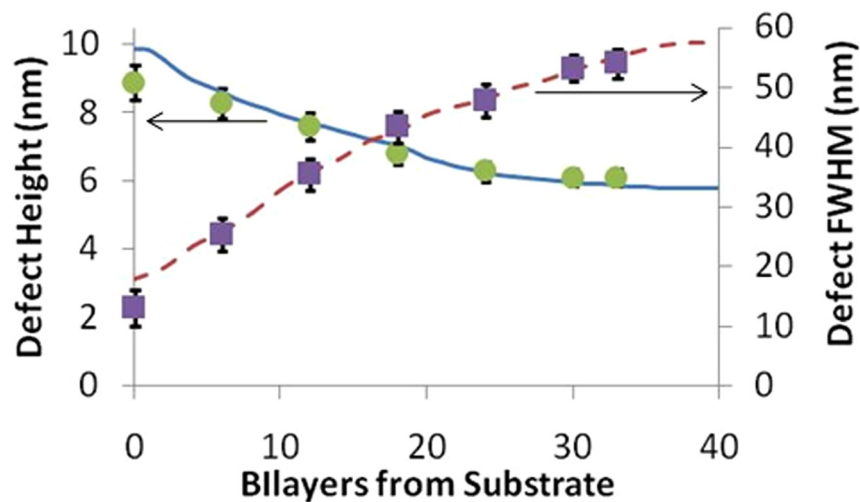

FIG. 5. (Color online) Change in width and height of the bump defect as a function of number of bilayers. Symbols (circles and squares) are values obtained from cross-section TEM image of the defect and the lines are obtained from the modeled multilayer growth. Error bars (representing standard deviation) shown are in nanometers.

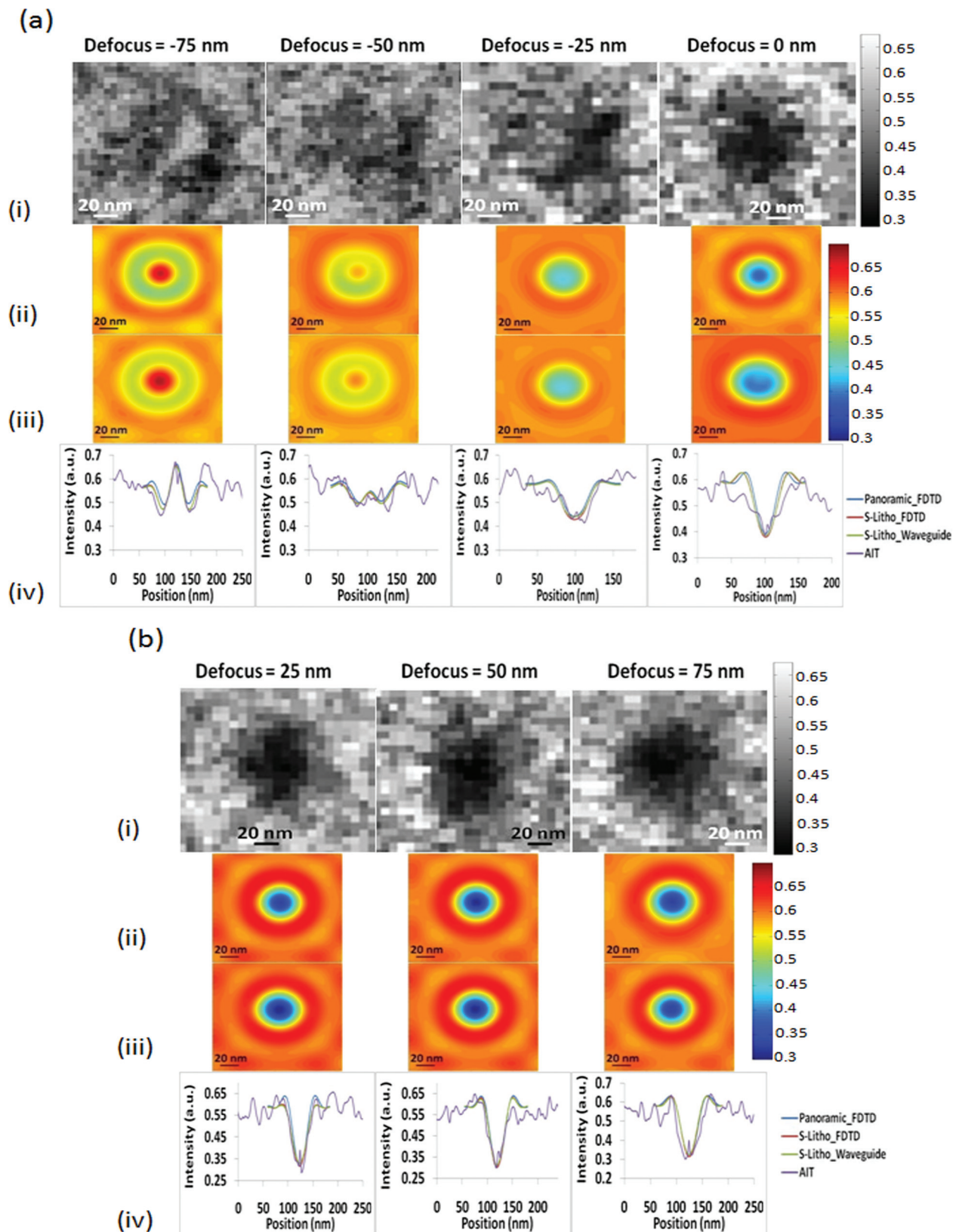**JVST B - Nanotechnology and Microelectronics: Materials, Processing, Measurement, and Phenomena**

FIG. 6. (Color) (a) and (b) (i) 2D aerial image intensity data obtained at AIT for the bump-type defect. (ii) 2D aerial image intensity data obtained with FDTD simulations performed using EM-Suite from Panoramic Technology Inc. (iii) 2D aerial image intensity data obtained with waveguide simulations performed using S-Litho from Synopsys. (iv) 1D aerial image intensity data extracted from the 2D aerial image intensity maps obtained at AIT, and those obtained using FDTD and waveguide simulations.
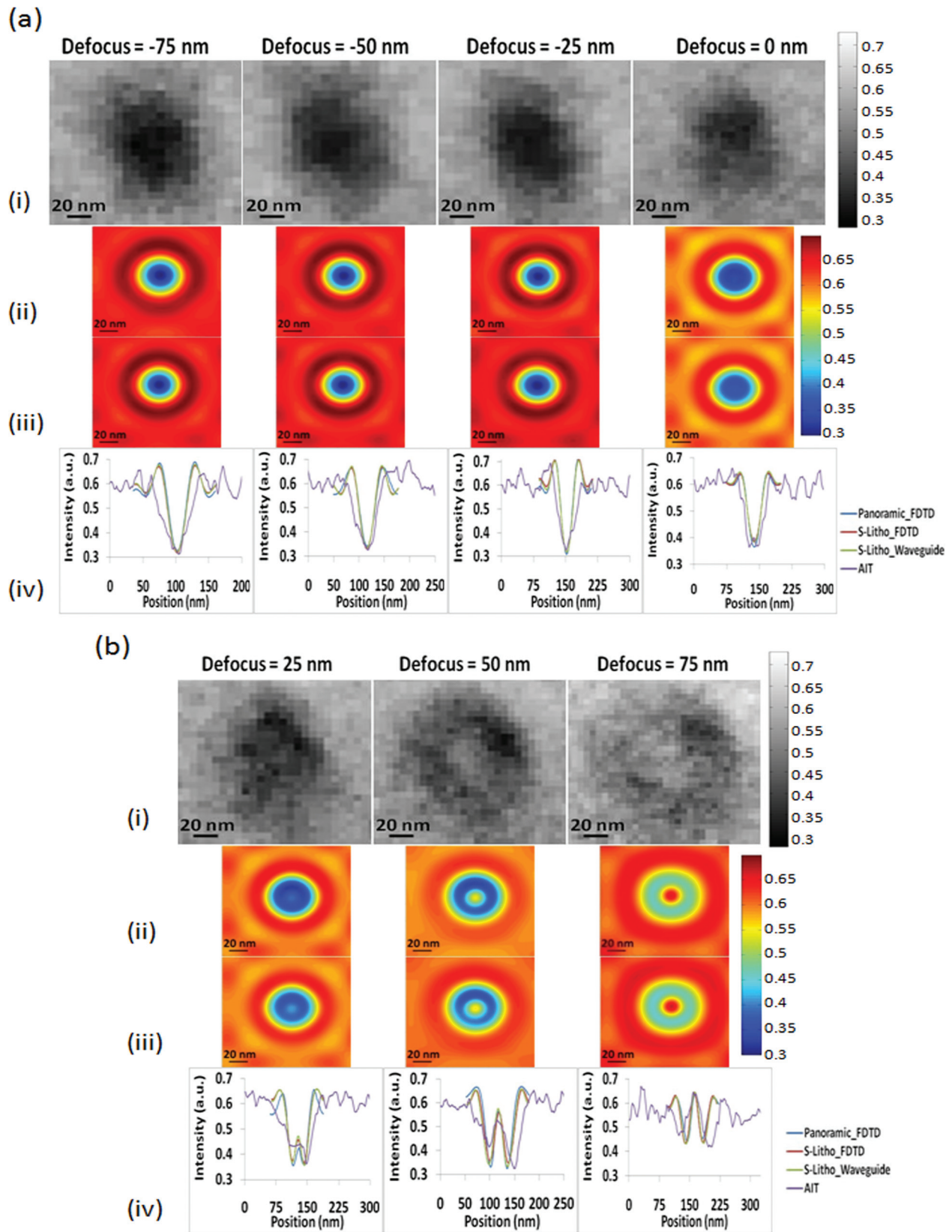
FIG. 7. (Color) (a) and (b) (i) 2D aerial image intensity data obtained at AIT for the pit-type defect. (ii) 2D aerial image intensity data obtained with FDTD simulations performed using EM-Suite from Panoramic Technology Inc. (iii) 2D aerial image intensity data obtained with waveguide simulations performed using S-Litho from Synopsys. (iv) 1D aerial image intensity data extracted from the 2D aerial image intensity maps obtained at AIT, and those obtained using FDTD and waveguide simulations.

relatively low EUV absorption by the defect, then normalization can be done using the average intensity across the entire field. The 1D aerial image intensity plots presented here were appropriately normalized and were obtained by taking cross-sections through the *x*-axis of the 2D aerial image intensity maps. The aerial image intensity data shown in Figs. 4 and 5 have been scaled to 4× wafer-side units. The difference in contrast (calculated by dividing the difference of maximum and minimum intensities by their sum) between AIT and simulated aerial image intensities for the various focus conditions was observed to be approximately 5% on average for both the bump and pit defects. Thus, we obtained a good match between the through-focus aerial image intensities obtained at AIT and those obtained using simulations. The FDTD simulations took almost 12 h to run while the waveguide simulations ran in around 1.5 min for simulating the 0.5 μm × 0.5 μm × 0.5 μm mask volume containing the characterized defects. The grid size (x × y × z, where *z* is the multilayer depth) used for all our simulations was 1 nm × 1 nm × 0.7 nm. No aberrations were included for our simulation work, as the AIT reported negligible aberrations during the time when our characterized defects were imaged.[22]

V. SUMMARY AND CONCLUSIONS

A realistic multilayer growth model was developed for the study of printing behavior of buried multilayer defects in EUV masks. The model takes into account the conditions of the ion beam deposition tool where the multilayer coating took place. A good match was obtained between the cross-section TEM profile of the multilayer disruption caused by the defects and the defect evolution up the multilayer stack, predicted by the growth model for both bump-type and pit-type defects. Also, the modeled defect profiles at the multilayer top were compared with the top-layer AFM defect measurements, and they agreed to within 1 nm in terms of both FWHM and height, for both the defects. Using the modeled multilayer growth as the input for our defect printability simulations, we found that the aerial image contrast of through-focus aerial image intensities obtained with the AIT matched those calculated using simulations to within approximately 4% on an average for the various focus conditions, for both the characterized native mask defects. The waveguide simulation was nearly 500 times faster than the

FDTD simulations for our characterized defects and yielded comparable results. This approach could be applied to the improvement of multilayer defect compensation techniques, and to actinic photomask inspection or qualification systems, like the EUV actinic aerial image metrology system.

[1]B. LaFontaine *et al.*, Proc. SPIE **6921**, 69210P (2008).
[2]O. Wood *et al.*, Proc. SPIE **7636**, 76361M (2010).
[3]S. Wurm, C.-U. Jeon, and M. Lercel, Proc. SPIE **6517**, 651705 (2007).
[4]P. B. Mirkarimi and D. G. Stearns, Appl. Phys. Lett. **77**, 2243 (2000).
[5]R. V. Randive, A. Ma, P. A. Kearney, D. Krick, I. Reiss, P. B. Mirkarimi, and E. Spiller, J. Micro/Nanolith **5**, 023003 (2006).
[6]Y. Lin and J. Bokor, J. Vac. Sci. Technol., B **15**, 2467 (1997).
[7]J. H-Jones, V. Jindal, P. Kearney, R. Teki, A. John, and H. J. Kwon, Proc. SPIE **8322**, 83221S (2012).
[8]T. Liang and E. Gullickson, International Symposium for EUV Lithography, Lake Tahoe, California, 25–27 September, 2008.
[9]B. T. Lee *et al.*, Proc. SPIE **4343**, 746 (2001).
[10]D. G. Stearns, P. B. Mirkarimi, and E. Spiller, Thin Solid Films **446**, 37 (2004).
[11]E. M. Gullikson, C. Cerjan, D. G. Stearns, P. B. Mirkarimi, and D. W. Sweeney, J. Vac. Sci. Technol., B **20**, 81 (2002).
[12]S. J. Osher and R. P. Fedkiw, *Level Set Methods and Dynamic Implicit Surfaces* (Springer, New York, 2003), Vol. 153.
[13]K. A. Goldberg, I. Mochi, P. Naulleau, T. Liang, P.-Y. Yang, and S. Huh, J. Vac. Sci. Technol., B **27**, 2916 (2009).
[14]V. Jindal, Ph.D. dissertation (State University of New York, 2008).
[15]V. Jindal, P. Kearney, J. Harris-Jones, A. Hayes, and J. Kools, Proc. SPIE **7969**, 79691A (2011).
[16]T. Cardinal, D. Andruczyk, H. Yu, V. Jindal, P. Kearney, and D. Ruzic, Proc. SPIE **8322**, 83222Q (2012).
[17]J. A. Sethian, Proc. Nat. Acad. Sci. U.S.A. **93**, 1591 (1996).
[18]S. Osher and J. A. Sethian, J. Comput. Phys. **79**, 12 (1988).
[19]K. S. Yee, IEEE Trans. Antennas Propag. **14**, 302 (1966).
[20]V. Domnenko, T. Klimpel, G. Viehoever, H. Koop, L. S. Melvin III, and T. Schmoeller, Proc. SPIE **6730**, 67304J (2007).
[21]K. D. Lucas, H. Tanabe, and A. J. Strojwas, J. Opt. Soc. Am. A **13**, 2187 (1996).
[22]K. A. Goldberg, I. Mochi, N. Smith, S. Rekawa, J. Macdougall, and P. Naulleau, *International Symposium on Extreme Ultraviolet Lithography*, Kobe, Japan, 17–20 October 2010.